

HOW DOES THE STELLAR WIND INFLUENCE THE RADIO MORPHOLOGY OF A SUPERNOVA REMNANT?

M. F. ZHANG,^{1,2} W. W. TIAN,^{1,2} AND D. WU^{1,2}

¹*Key Laboratory of Optical Astronomy, National Astronomical Observatories, Chinese Academy of Sciences, Beijing 100012, China*

²*University of Chinese Academy of Sciences, 19A Yuquan Road, Shijingshan District, Beijing 100049, China*

ABSTRACT

We simulate the evolutions of the stellar wind and the supernova remnant (SNR) originating from a runaway massive star in an uniform Galactic environment based on the three-dimensional magnetohydrodynamics models. Taking the stellar wind into consideration, we can explain the radio morphologies of many supernova remnants. The directions of the kinematic velocity of the progenitor, the magnetic field and the line of sight are the most important factors influencing the morphologies. If the velocity is perpendicular to the magnetic field, the simulation will give us two different unilateral SNRs and a bilateral symmetric SNR. If the velocity is parallel to the magnetic field, we can obtain a bilateral asymmetric SNR and a quasi-circular SNR. Our simulations show the stellar wind plays a key role in the radio evolution of a SNR, which implies the Galactic global density and magnetic field distribution play a secondary role in shaping a SNR.

Keywords: ISM: supernova remnants – ISM: magnetic fields – magnetohydrodynamics

arXiv:1810.03777v1 [astro-ph.GA] 9 Oct 2018

1. INTRODUCTION

A massive star dies, then forms a supernova remnant (SNR). This process produces heavy elements, dusts and cosmic rays, which has important impact on the Galactic interstellar medium (ISM). To understand this process, we need study the evolution of SNRs. Truelove & McKee (1999) and Cioffi et al. (1988) did many analytical and numerical calculations about the evolution. Comparing the results with the observations, they developed a practical model. However, there is usually the diverse surrounding environment which will influence the evolution of SNRs. As a result, the radio morphologies of SNRs are various. The practical model can explain some regular morphologies, such as bilateral symmetric and circular SNRs, but is powerless to explain more complex morphologies. These morphologies can help us infer some important natures of SNRs, so it is significant to study them in detail.

The numerical simulation is an effective method to describe the surrounding environment and obtain the evolution images of a SNR at different phases. With the improvement of the computation ability, the two-dimensional (2D) hydrodynamics (HD) simulation shows its power in studying the magnetic amplification, the diffusive shock acceleration and the instability of SNRs (Jun & Norman 1996; Kang & Jones 2006; Fang & Zhang 2012). Recently, we can perform three-dimensional (3D) simulations, and also convert the simulation results to radio, optical or X-ray images in order to compare with observations (Orlando et al. 2007; Meyer et al. 2015; Zhang et al. 2017). Orlando et al. (2007) tried to explain asymmetric morphologies of some bilateral supernova remnants by assuming inhomogeneous density and magnetic field. They simulated some asymmetric structures in SNRs, but did not describe how the assuming surrounding environment is formed around the SNRs. West et al. (2016) thought the surrounding environments are mainly influenced by the Galactic global ISM distribution and applied a method of magnetohydrodynamics (MHD) simulation to study the Galactic magnetic field model. They partly explains the assumed surrounding environments by Orlando et al. (2007), but cannot well simulate many asymmetric structures. Thus, there should probably be another factor influencing the surrounding environments.

This factor is possibly the stellar wind of the progenitor. The progenitor runs in the ISM and blows a stellar wind bubble, which leads to inhomogeneous density distribution and magnetic field structure. This certainly influences the following remnant's evolution and its radio morphology when a supernova explodes in

such a bubble. This assumption is self-consistent and supported by theoretical calculations and observations (Chen et al. 1995; Zhang et al. 1996; Foster et al. 2004; Lee et al. 2010). Meyer et al. (2015) simulated the stellar wind, then took the result as the initial condition of the SNR simulation. They concluded that the stellar wind will strongly shape the density distribution of the SNRs. They only performed the 2D HD simulations and did not obtain the radio images. The crucial parameters of the 3D MHD simulation include the density and the magnetic field of the ISM, the spatial velocity and the stellar wind of the progenitor, the explosion energy and the mass of the supernova. It is impossible to test all combinations of these parameters by now. In particular, there are two vectorial parameters, the magnetic field of the ISM and the velocity of the progenitor. Each vector has three components, which largely complicates the conditions that one has to take into account for the 3D simulation.

We in the paper present a 3D MHD simulation where these parameters are fixed but the relative directions of the magnetic field and the velocity of the progenitor. We perform two simulations, one for the magnetic field in perpendicular to the velocity, one for the magnetic field in parallel to the velocity. In the following text, we call the former the perpendicular simulation and the latter the parallel simulation. Using canonical values of a massive star, we may obtain many radio morphologies of SNRs based on such a simplification. We also count different types of SNRs, so that we can better understand our simulation results.

In Sect.2, we describe the simulation model and list the parameters we use. In Sect.3, we present and discuss the results. Sect.4 is a summary.

2. SIMULATION MODEL

The simulation model is based on a 3D MHD frame with a grid of $128 \times 128 \times 128$. The spatial scale is set to $60 \text{ pc} \times 60 \text{ pc} \times 60 \text{ pc}$, i.e. its resolution is $0.47 \text{ pc pixel}^{-1}$. The viscosity and the gravitation have little influence on the simulation, so we ignore them. The cooling and heating effect mainly influences the luminosity of optical and X-ray radiation, and we mainly focus radio radiation, so they are not included in the simulation. In the stellar wind simulation, the thermal conduction is an important process (Meyer et al. 2014b), which can govern the shape, the size and the structure of the stellar winds. However, it is not the dominant factor in the SNR simulation, so we only discuss its influence in the perpendicular simulation. The simulation

is based on the ideal conservation equation set:

$$\begin{cases} \frac{\partial \rho}{\partial t} + \nabla \cdot (\rho \mathbf{v}) = 0, \\ \frac{\partial \rho \mathbf{v}}{\partial t} + \nabla \cdot (\rho \mathbf{v} \mathbf{v} - \mathbf{B} \mathbf{B}) + \nabla P^* = 0, \\ \frac{\partial E}{\partial t} + \nabla \cdot [(E + P^*) \mathbf{v} - \mathbf{B}(\mathbf{v} \cdot \mathbf{B})] = 0, \\ \frac{\partial \mathbf{B}}{\partial t} + \nabla \times (\mathbf{v} \times \mathbf{B}) = 0, \end{cases} \quad (1)$$

in which, ρ is mass density, \mathbf{v} is velocity, \mathbf{B} is magnetic field intensity, P^* is total pressure, and E is total energy density.

The simulation contains two models, the stellar wind model and the supernova remnant model. At first, we simulate the evolution of the stellar wind, and the results are taken as the initial conditions in the SNR simulation. Then we perform the SNR simulation and convert the results to relative radio flux density images. Finally, we compare the simulation radio images with the observed radio images.

We perform the simulations using a code, PLUTO¹ (Mignone et al. 2007, 2012), and summary the parameters in Table. 1. The parameters that we do not show the references are just the canonical values we estimate.

2.1. The stellar wind model

How the stellar winds of runaway massive stars evolve is still an unsolved problem, so we only use a reasonable simplified model. If the stellar winds can influence the SNRs obviously, their spatial scales should be similar to SNRs. The typical diameters of SNRs are usually several parsecs (pcs). Meyer et al. (2014b) showed that the mass of the star should be at least $40 M_{\odot}$ to reach such a scale, if the speed of the star is 40 km s^{-1} . Lower mass means lower speed (Mackey et al. 2015), but lower speed means lower asymmetry, which is inconsistent with the aim of this paper. We therefore choose the mass $40 M_{\odot}$ and the speed 40 km s^{-1} as the initial parameters in our simulation. It is known that the star's life is composed of the main sequence (MS) and the red supergiant (RSG) phase. However, our tests show the stellar wind in main sequence phase has little impact on the evolution of a SNR, so we only simulate it for the last one million years.

The mass loss of a $40 M_{\odot}$ star usually varies from 1×10^{-6} to $1 \times 10^{-5} M_{\odot} \text{ yr}^{-1}$ during the last one million years of the star's life (Meyer et al. 2014b; van Marle et al. 2012, 2015), so we use a mass-loss rate of $3 \times 10^{-6} M_{\odot} \text{ yr}^{-1}$ for simplicity. Here we warn readers that it is not reality to accurately estimate the mass-loss rate of a massive star so far (Meyer et al. 2014a;

Table 1. Summary of Simulation Parameters

Parameters	Value	References
Stellar Wind Parameters		
Progenitor Velocity	40 km s^{-1}	1
Mass-Loss Rate	$3 \times 10^{-6} M_{\odot} \text{ yr}^{-1}$	2
Stellar Wind Velocity	800 km s^{-1}	2
Stellar Wind Density	0.05 cm^{-3}	2
Inner Radius	0.5 pc	
Evolution Time	1 million years	1
SNR Parameters		
Ejecta Mass	$15.3 M_{\odot}$	3
Initial Explosion Energy	$1.3 \times 10^{51} \text{ ergs}$	4, 5
Initial Radius	4 pc	
Initial Time	650 years	6
Other Parameters		
Mean Density	0.5 cm^{-3}	7, 8
Magnetic Field Intensity	$9 \mu\text{G}$	9
Mean Atomic Weight	1.3	
Adiabatic Coefficient	1.7	
Synchrotron Index (β)	0.5	

References—(1)Meyer et al. 2014b; (2)Meyer et al. 2015; (3)Sukhbold et al. 2016; (4)Poznanski 2013; (5)Müller et al. 2016; (6)Leahy & Williams 2017; (7)Nakanishi & Sofue 2006; (8)Nakanishi & Sofue 2016; (9)Haverkorn 2015

Gvaramadze et al. 2014). Also, we set the inner radius as 0.5 pc, i.e. the stellar wind is generated from such a small region in the simulation. This radius is large enough to guarantee the wind blows spherically in the square grid of numerical simulation and small enough to be consistent with the simplified stellar wind model. The mass-loss rate \dot{M} , the inner radius r , the velocity v and the mass density ρ of the stellar wind are linked by

$$\dot{M} = 4\pi r^2 \rho v. \quad (2)$$

The initial velocity of the stellar wind originating from the progenitor will not change in 0.5 pc, if we assume it propagates freely in such a short radius. Then the velocity should be about 800 km s^{-1} and the density is about 0.05 cm^{-3} (Meyer et al. 2014b).

In addition, we set the initial surrounding environment before the stellar wind evolution. We assume the ISM is ideal gas, where the mean atomic weight is 1.3 and the adiabatic coefficient is 1.7. We set a uniform magnetic field of $9 \mu\text{G}$ (Haverkorn 2015) and a uniform ISM number density of 0.5 cm^{-3} (Nakanishi & Sofue

¹ <http://plutocode.ph.unito.it/>

2006, 2016), the typical values of the Galactic ISM. The environment is usually inhomogeneous, which will result in a more complex radio morphology in the simulation. However, we only want to test how the SNRs are influenced by the stellar winds, so we use a homogeneous ISM in this work.

2.2. The supernova remnant model

The evolution of a SNR is divided into three phases, the ejecta-dominated (ED) phase, the Sedov-Taylor (ST) phase and the pressure-driven snowplow (PDS) phase (Truelove & McKee 1999). The first two phases are classified as "nonradiative", but the radiative loss becomes important in the PDS phase. Our simulations only cover the first two phases, so we do not need to estimate radiative loss. For a $40 M_{\odot}$ star, the ejecta mass is about $15.3 M_{\odot}$ (Sukhbold et al. 2016) and the explosion energy is about 3.6×10^{51} erg according to the function (Poznanski 2013; Müller et al. 2016),

$$\log(E/10^{50} \text{erg}) = 2.09 \log(M_{ej}/M_{\odot}) - 1.78. \quad (3)$$

To simulate a spherically symmetric explosion, we set an initial radius as 4 pc. The shock wave of the supernova explosion will spend 650 years to reach 4 pc. Because the ST phase starts from 1365 years for such a star (Leahy & Williams 2017), it is still in ED phase. Therefore, we can obtain the 650-years evolution directly from the existed theory (Truelove & McKee 1999) which gives the density, pressure and velocity profile. The magnetic field is not important at this time, so we ignore it here. In short, the initial conditions are the evolution results after 650 years.

Next we start to simulate the evolution of a SNR in the surrounding environment blown by the stellar wind. Our simulation has shown the density, the magnetic field, the velocity and the pressure in the whole simulation space. We further convert these simulation results into radio images in order to compare with real observations.

Assuming the radio emission is totally from synchrotron mechanism, we obtain the radio flux volume density by employing $i(\nu) = C \rho B_{\perp}^{\beta+1} \nu^{-\beta}$ (Orlando et al. 2007), in which ν is the radiation frequency, C a constant, ρ the density, B_{\perp} the magnetic field perpendicular to the line of sight (LoS) and β the synchrotron spectral index. The absolute radio flux density is dependent on the constant C , but C contains electron acceleration efficiency which is difficult to be obtained. Moreover, the $\nu^{-\beta}$ is also excluded from the equation, because it is meaningless if we do not want to calculate the absolute radio flux density. As a result, the final equation used in this work is $i(\nu) = \rho B_{\perp}^{\beta+1}$. Then we integrate the $i(\nu)$

along the LoS to obtain relative radio flux density. The resolution of the simulation is usually higher than the observation, so we smooth the simulation radio images by using a 2D Gaussian function with $\sigma = 1$.

3. RESULTS AND DISCUSSION

We show the results and compare them with the observations in this section.

Based on West et al. (2016)'s collection of all radio SNRs' images, we classify the SNRs to seven types: unilateral small-radian, unilateral large-radian, bilateral symmetric, bilateral asymmetric, multi-layers, circular and irregular. A multi-layers SNR means there are two or more layers on one or two sides. The typical multi-layers, circular and irregular SNRs are shown in Figure 1. The statistics of the seven types is listed in Table 2. We only select 288 SNRs in this statistics, because other images are obscure. However, we list all samples except for the irregular type for the convenience of readers.

3.1. Perpendicular Simulation

The perpendicular simulation is shown in Figure 2. The top panels show the initial conditions at three directions. It is composed of two parts, the surrounding environment and the inner supernova explosion region. The surrounding environment results from the stellar wind evolution and the inner's physics status is calculated based on the work of Leahy & Williams (2017). The initial magnetic field and the progenitor velocity are set to follow the y-axis and z-axis respectively. This leads to an obvious bow structure in y-z plane and the very chaotic magnetic field in x-z plane. To make the patterns clearer, the white arrows and the pattern colors are set with different scales in different images. The values labeled on the color bar are absolute, so they can be used to compare the densities in different images.

The second row of Figure 2 shows the SNR simulation results after 1200 years. If we add the initial 650 years, then the age of this artificial SNR is 1850 years. The radio morphologies, shown in the third row, are a little surprising, especially in x-z plane. Our simulations can simultaneously result in the bilateral symmetric, the unilateral big-radian and small-radian SNRs. As a comparison, three real SNRs (West et al. 2016) are shown in the bottom panels of Figure 2. This proves that three kind of SNRs may originate from same a progenitor, and their morphologies depend on the view angle at which we see them. The bilateral symmetric SNRs have been well studied by simulations and observations (Gaensler et al. 1999; Petruk et al. 2009), but there are still many ambiguities for unilateral SNRs. Here we show the im-

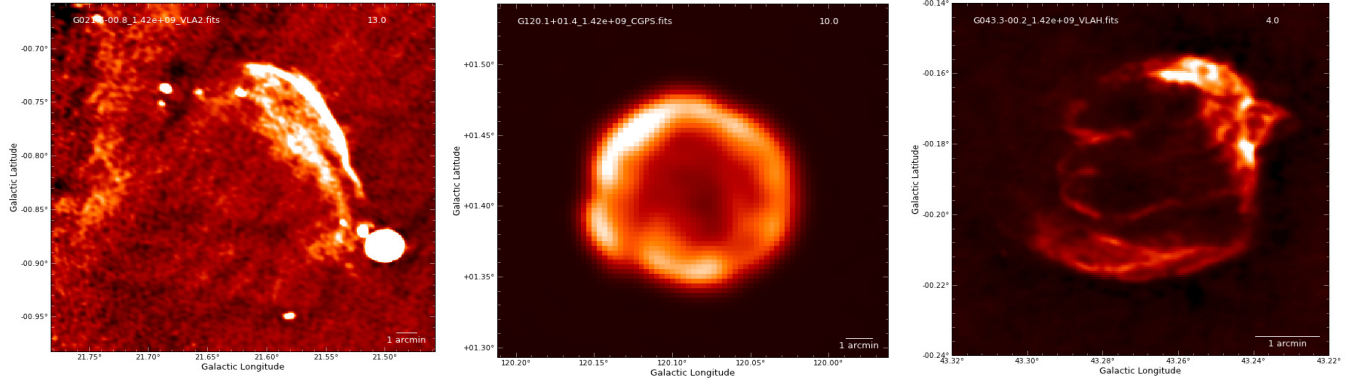


Figure 1. The typical multi-layers, circular and irregular SNRs: G21.6-0.8, G120.1+1.4 and G43.3-0.2, respectively.

Table 2. Statistics of different SNRs

Types	Numbers	Samples
unilateral small-radian	35	G4.2-3.5, G5.9+3.1, G6.1+0.5, G6.4+4.0, G7.0-0.1, G7.2+0.2, G11.1+0.1, G11.1-0.7, G12.2+0.3, G14.3+0.1, G17.4-0.1, G24.7-0.6, G49.2-0.7, G57.2+0.8, G59.8+1.2, G65.1+0.6, G310.8-0.4, G327.4+1.0, G338.1+0.4, G348.5-0.0, G348.7+0.3, G350.0-2.0, G351.7+0.8, G351.9-0.9, G354.1+0.1, G359.0-0.9
unilateral large-radian	15	G0.0+0.0, G1.9+0.3, G3.8+0.3, G8.3-0.0, G9.8+0.6, G18.6-0.2, G18.8+0.3, G33.2-0.6, G55.7+3.4, G66.0-0.0, G116.9+0.2, G119.5+10.2, G298.6-0.0, G321.9-1.1, G342.1+0.9
bilateral symmetric	17	G0.9+0.1, G1.0-0.1, G3.7-0.2, G8.7-5.0, G16.2-2.7, G21.0-0.4, G23.3-0.3, G36.6+2.6, G59.5+0.1, G65.3+5.7, G296.5+10.0, G321.9-0.3, G327.6+14.6, G332.0+0.2, G349.2-0.1, G353.9-2.0, G356.3-1.5
bilateral asymmetric	11	G11.0-0.0, G21.8-0.6, G29.7-0.3, G42.8+0.6, G53.6-2.2, G54.4-0.3, G64.5+0.9, G304.6+0.1, G348.5+0.1, G350.1-0.3, G352.7-0.1
multi-layers	13	G21.6-0.8, G24.7+0.6, G46.8-0.3, G85.4+0.7, G93.3+6.9, G109.1-1.0, G284.3-1.8, G286.5-1.2, G318.9+0.4, G320.6-1.6, G327.4+0.4, G358.1+1.0, G358.5-0.9
circular	42	G4.5+6.8, G5.2-2.6, G6.5-0.4, G11.2-0.3, G11.4-0.1, G15.9+0.2, G16.7+0.1, G18.1-0.1, G21.5-0.9, G27.4+0.0, G69.7+1.0, G82.2+5.3, G83.0-0.3, G84.2-0.8, G111.7-2.1, G120.1+1.4, G132.7+1.3, G179.0+2.6, G180.0-1.7, G184.6-5.8, G261.9+5.5, G290.1-0.8, G299.2-2.9, G301.4-1.0, G302.3+0.7, G308.1-0.7, G310.6-0.3, G311.5-0.3, G315.4-2.3, G322.5-0.1, G326.3-1.8, G327.1-1.1, G327.2-0.1, G332.4-0.4, G337.3+1.0, G346.6-0.2, G354.8-0.8, G355.6-0.0, G355.9-2.5, G356.2+4.5, G358.0+3.8, G359.1-0.5
irregular	155	

ages toward three directions, but in fact the SNR morphology varies following different view angle. We take SNR G116.9+0.2 as an example here. If we rotate 45° along the z-axis, we can get a unilateral bigger-radian morphology SNR in z-xy plane (see Figure 3), which is more similar to the SNR G116.9+0.2. Moreover, the magnetic field of G116.9+0.2 is parallel to the shell (Sun et al. 2011) in the polarization observation, which is totally different from the result in x-z plane. However, if

we rotate 45° along the z-axis, the magnetic field becomes similar to the observation (see Figure 4). The X-ray emission region of G116.9+0.2 is extended away from the radio shell (Pannuti et al. 2010), which is also revealed by our simulation (see Figure 5). In the left panel of Figure 5, the bottom high-temperature region is low-density comparing with the middle panel of the second row of Figure 2, which hints it is a high-temperature low-density region full of ionized gas. This is an ap-

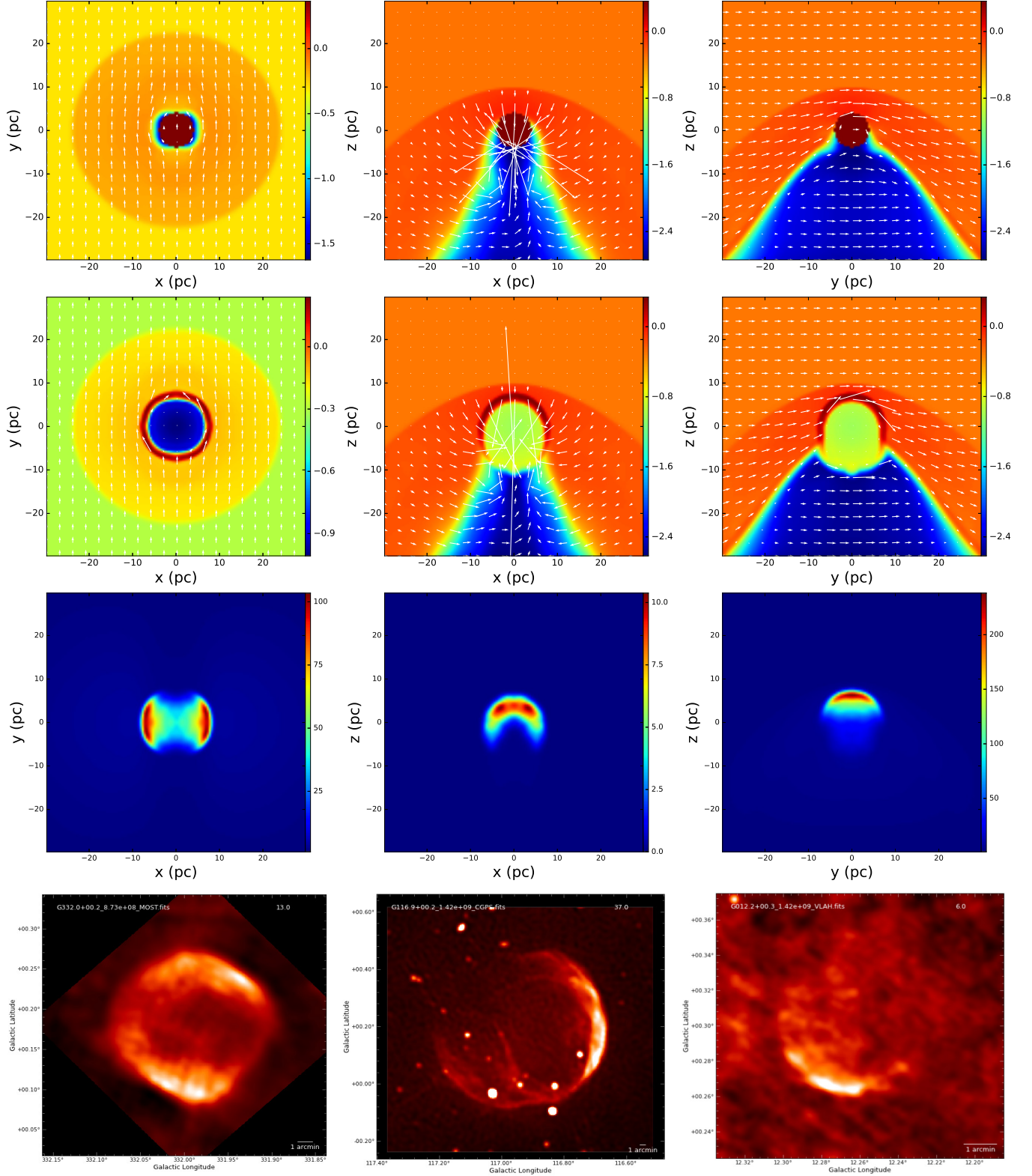


Figure 2. Simulation images assuming the velocity is perpendicular to the magnetic field. Top three images show the stellar wind simulation results at different views. The second row shows the SNR simulation results which apply the top three images as the initial conditions. The third row shows the relative radio flux density converted from the second row. The last row shows the real observed radio images of SNRs, G332.0+0.2, G116.9+0.2 and G12.2+0.3 (West et al. 2016). The three SNRs are bilateral symmetric, unilateral large-radian and unilateral small-radian, respectively. In the top two rows, the colorful patterns indicate the density distribution with a unit of $\log(\text{cm}^{-3})$. The length and the direction of the white arrows respectively indicate the intensity and the direction of magnetic field.

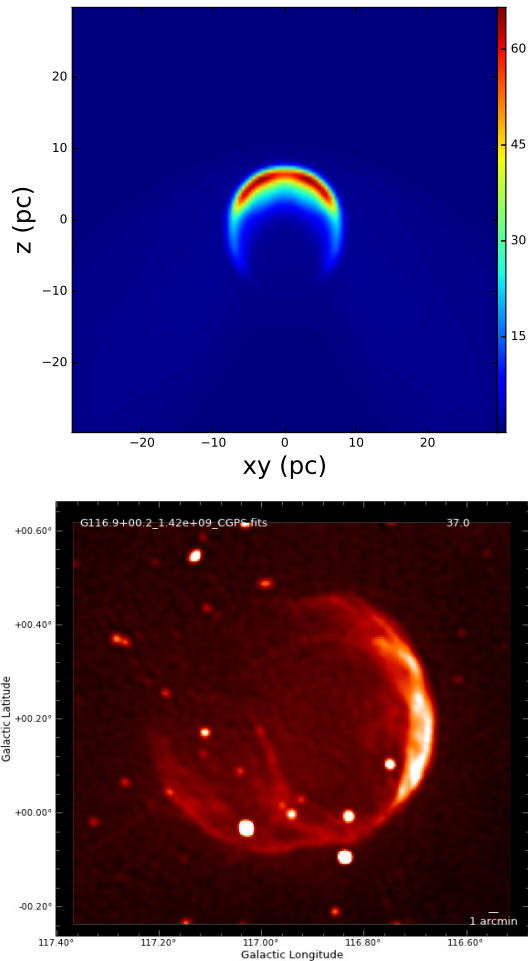


Figure 3. The simulated radio image after rotating 45° along z-axis and the observed radio image of SNR G116.9+0.2 (West et al. 2016; Tian & Leahy 2006).

appropriate environment to generate X-ray emission by bremsstrahlung mechanism. Therefore it is possible that the high speed of the progenitor leads to the extensive X-ray emission. Craig et al. (1997); Yar-Uyaniker et al. (2004); West et al. (2016) have ever tried to explain the X-ray morphology, but have not come to the conclusion. A more specific simulation for SNR G116.9+0.2 will help us further understand it.

It is worthy to be mentioned that we do not add a magnetic field gradient or a density gradient at the beginning. Even if the initial ISM is uniform, we can still obtain various morphologies. In other words, the radio morphology is not only dependent on the initial ISM distribution. Therefore, it is unreasonable to estimate the initial magnetic field or density distribution before the progenitor formation based on the radio morphology of a SNR. Also the radio morphology should not be used to infer the large-scale magnetic field or density distribution in Milky Way, since the local environment

has been changed by the stellar wind, which leads to the difference between local and large-scale environment. In fact, Orlando et al. (2007) obtained similar radio morphologies based on inhomogeneous initial ISM settings, but they did not explain the origin of such initial conditions. van Marle et al. (2010) took the stellar wind into consideration and explained the its influences based on HD simulations, but did not get radio images. Moreover, they both did not consider the motion of the progenitor. It is well-known that most of stars are moving against the surrounding environment, so our work is a meaningful supplement to the previous research. In fact, aiming at particular SNRs, Vigh et al. (2011) tried to study the asymmetries of Tycho SNR, while Schneider et al. (2006) generated the morphology of SNR 3C 400.2 and discussed the effect of the thermal conduction. Toledo-Roy et al. (2014a) took the motion of the progenitor into consideration and well explained the morphology of Kepler SNR by including the stellar wind. Further, Toledo-Roy et al. (2014b) combined the X-ray and radio emissions and studied SNR G352.70.1 based on a MHD simulation, but they did not consider the stellar wind and the motion of the progenitor in their study.

Figure 2 has shown that the relative flux densities in different planes are different. The flux density is low in x-z plane, and higher in x-y plane, then the highest in y-z plane. So it is reasonable that the unilateral small-radian SNRs appear more frequent than the unilateral big-radian SNRs, because bright SNRs are easier to be detected. Such a derivation is supported by the statistics of the SNR morphologies (see Table. 2). Therefore there should exist more undiscovered unilateral big-radian SNRs in our Galaxy. The third row of Figure 2 shows that the top flux density of y-z plane is about 20 times larger than that in the x-z plane, so it is possible to detect more unilateral big-radian SNRs once we get the sensitivity 20 times better. The fact that the number of the observed SNRs (about 300, see Green (2014)) is much less than the theory prediction of above 1000 by now (Frail et al. 1994; Tammann et al. 1994), can be partly explained by the simulation results.

We also try to check the influence of thermal conduction in the simulation, because the thermal conduction plays an important role in the evolution of stellar wind (Meyer et al. 2014b). We apply the explicit scheme and the standard thermal conduction coefficients in the code PLUTO. Figure 6 shows our simulation results. The simulation reveals that the bow shell has two layers and the magnetic field is also different from that without the thermal conduction (see Figure 2). Meyer et al. (2015) showed the effects on the mixing of material, which is not obvious in our work, because we use different param-

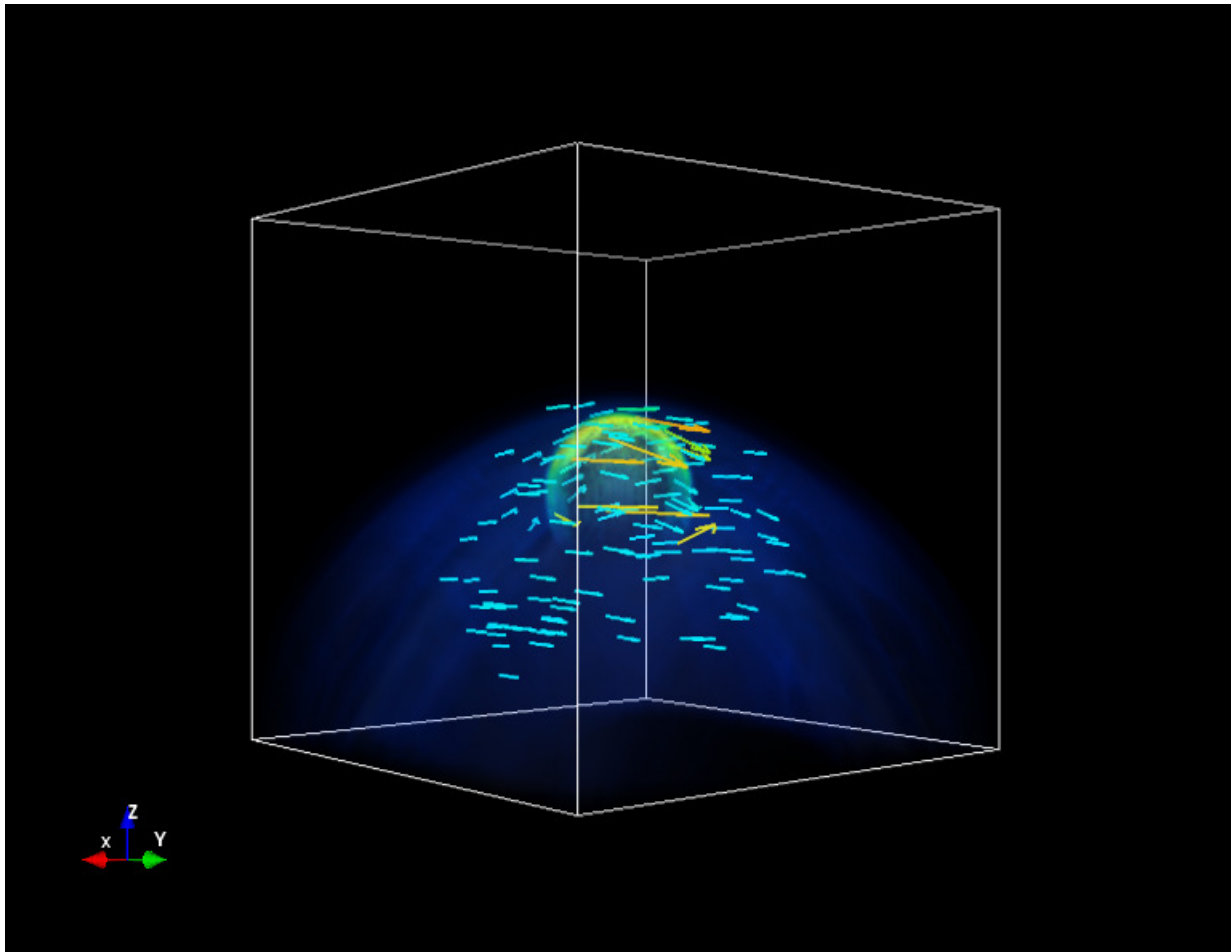


Figure 4. The simulation 3D image after rotating 50° along z-axis from the x-z plane. If we rotate it 45° , the middle two vertical outlines will overlap with each other. Thus, we rotate a little more to make it more distinct. The colorful patterns indicate the relative radio flux density. The yellow shows the high flux density. The arrows show the magnetic field. A more yellow arrow means the larger magnetic intensity. (This figure is available online as an animation.)

ters. The simulation including thermal conduction does not show obvious change in the density and magnetic field evolution around the SNR. The radio morphologies are similar to those in Figure 2, so we do not show them. In conclusion, the thermal conduction plays a small role in the radio evolution of a SNR.

3.2. Parallel Simulation

The parallel simulation is shown in Figure 7. All initial parameters are same as the perpendicular simulation and the age is also 1850 years. We warn that the stellar wind region shows obvious radio emission, which is wrong, because there is no relativistic electron in the stellar wind region and synchrotron mechanism is here not important. However, it is impossible for us to exclude it from the radio images, because we do not know the boundary of the relativistic electrons region. This flaw also influences other simulation radio images. We only show the y-z plane in Figure 7, because the x-z

plane is same as the y-z plane. Moreover, we should see a circular SNR in the x-y plane but in fact a square SNR in our simulation, because the resolution is not high and every pixel is square. The stellar wind simulation is time-consuming, so we selectively set a reasonable resolution.

Figure 7 shows that the radio morphology is a bilateral asymmetric SNR. [van Marle et al. \(2014a\)](#) showed that the magnetic field would shape the stellar wind nebulae of asymptotic giant (AGB) stars as bilateral symmetric morphologies. Including the motion of AGB stars, [van Marle et al. \(2014b\)](#) studied the instabilities in such a system. [Meyer et al. \(2017\)](#) also simulated the bow shock nebulae of hot massive stars in a magnetized medium, which shows similar results as our parallel stellar wind simulation. However, they did not add the supernova explosion and convert the results to radio images. Taking the circular SNR into account, we are able to simulate five types of SNRs in our classification. Only

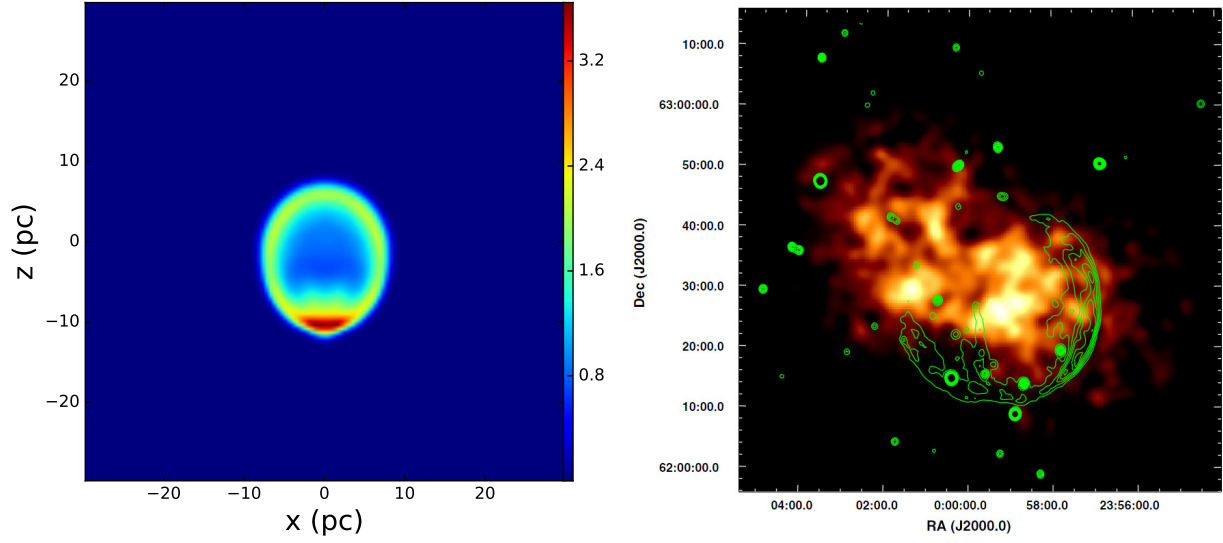


Figure 5. *Left:* the relative temperature distribution in x - z plane. *Right:* ASCA (Advanced Satellite for Cosmology and Astrophysics) X-ray image of G116.9+0.2 with CGPS (Canadian Galactic Plane Survey) radio contours overlaid (from Pannuti et al. (2010)).

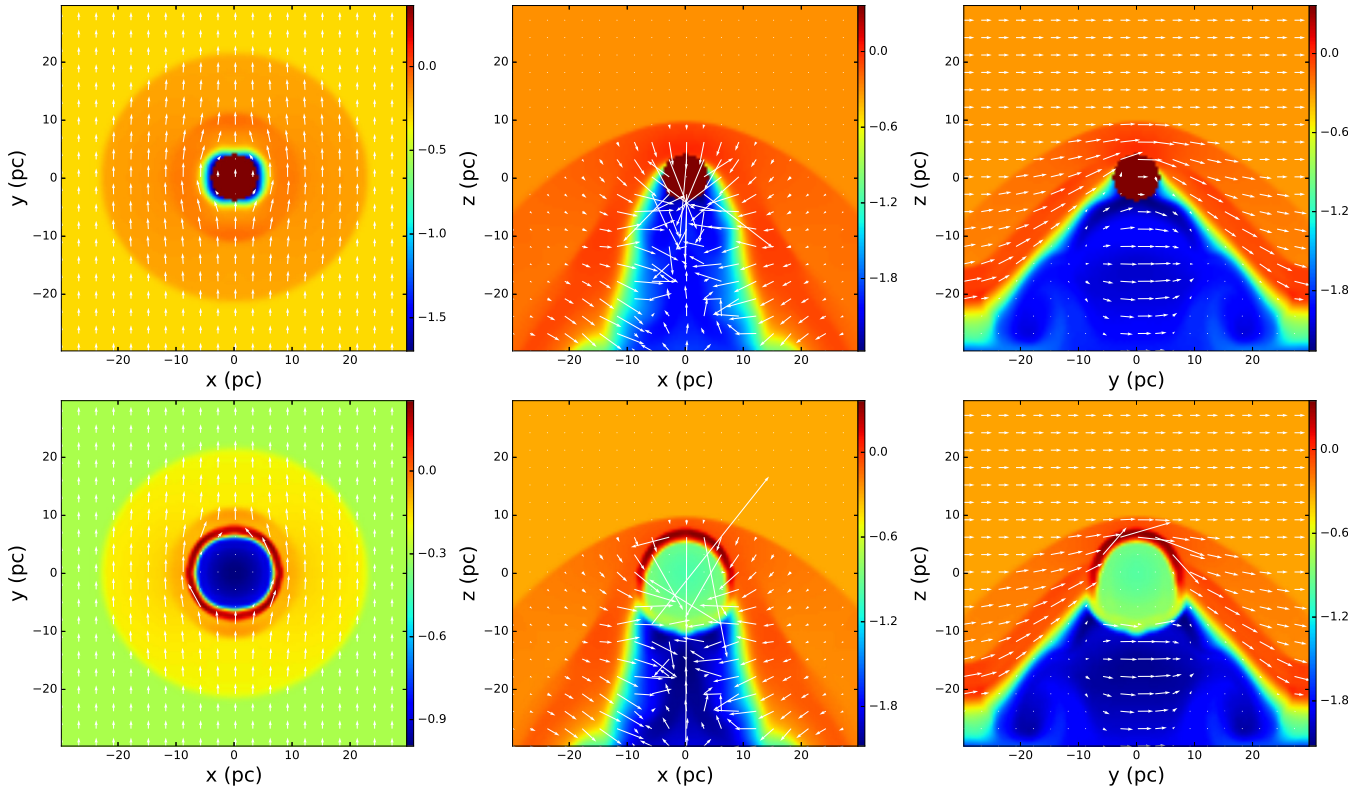


Figure 6. Simulation images with thermal conductions. They are similar to the top two rows of Figure 2. The only difference is that the thermal conduction is included in the simulation.

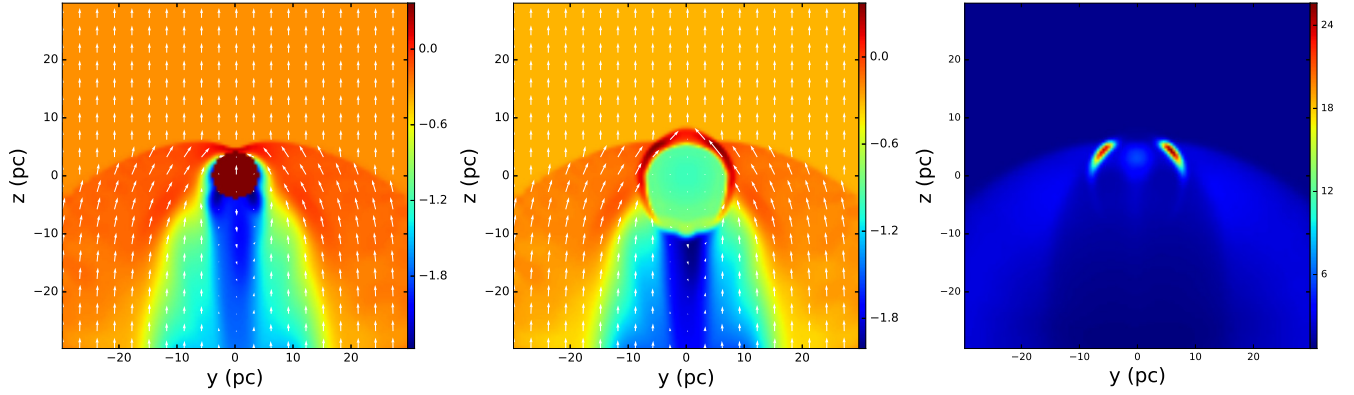


Figure 7. Simulation images assuming the velocity is parallel to the magnetic field. The left panel shows the stellar wind simulation result at y - z plane. The middle panel shows the SNR simulation result at y - z plane. The right panel shows the relative radio flux density converted from the middle panel.

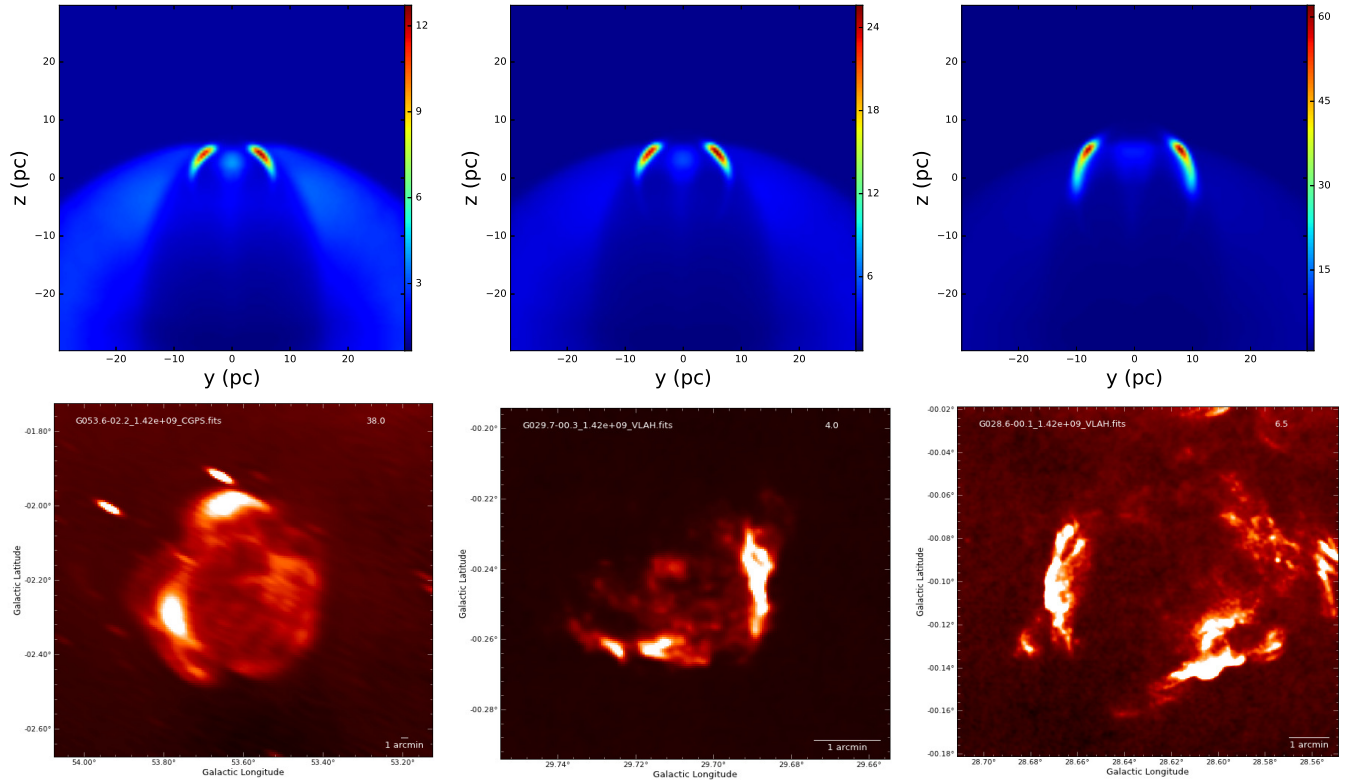


Figure 8. The upper three images show the simulation relative radio flux density at different ages. The lower images show the observed radio images of SNRs, G53.6-2.2, G29.7-0.3 and G28.6-0.1 (West et al. 2016), all of which are bilateral asymmetric.

the multi-layers and the irregular SNRs are difficult to be simulated. Their formations are likely influenced by the inhomogeneous initial surrounding environment or the unusual progenitor (Orlando et al. 2007, 2017).

The upper images of Figure 8 show the simulation morphologies at 1450, 1850 and 3050 years respectively. As a comparison, three real SNRs, G53.6-2.2, G29.7-0.3, G28.6-0.1, are shown in the lower panels of Figure 8. Because of the similar morphologies between the simulation images and the observation images, the three SNRs are likely all few thousands years old. In fact, G29.7-0.3 is about one thousands years old (Leahy & Tian 2008) and G28.6-0.1 (Bamba et al. 2001) is no more than 2700 years old. G53.6-2.2 seems older (about 15,000 years old, see Long et al. (1991)), which is worthy to be further checked. In addition, the X-ray emissions of the three SNRs are all more or less separated from the radio shell (Broersen & Vink 2015; Su et al. 2009; Bamba et al. 2001), similar to SNR G116.9+0.2. The simulation results also coincide with these observations, just like the perpendicular simulation for G116.9+0.2 so we do not show them here.

Since the parameters are same at the two simulations, we are able to compare the relative flux density in parallel with that in perpendicular simulations at same age. Figure 7 shows the relative flux density in the y-z plane for the parallel simulation is much lower than that for the perpendicular simulation. In other words, bilateral asymmetric SNRs should be less than unilateral small-radian SNRs. This is supported by the statistics in Table. 2. The unilateral large-radian SNRs should be less than the bilateral asymmetric SNRs, if we only take the x-z plane into consideration in the simulation results. However, the directions of the LoS might influence this estimation. For example, the Figure 3 shows a unilateral large-radian SNR is brighter than the bilateral asymmetric SNR. In fact, Table. 2 implies that the unilateral large-radian SNRs are more than the bilateral asymmetric SNRs.

4. SUMMARY

Taking the evolution result of the stellar wind as the initial conditions, we simulate the SNR evolution of a runaway $40 M_{\odot}$ progenitor star. The stellar wind simulations includes two models, the perpendicular simulation and the parallel simulation. Based on real radio morphologies, we classify the SNRs into seven types. Our conclusions are summarized as follows:

1. The stellar wind of the massive progenitor plays a key role in shaping the radio morphologies of SNRs, and is possibly important more than the initial surrounding environment.
2. Considering the stellar wind, we can explain many radio morphologies of SNRs, except for the multi-layers and irregular SNRs.
3. It is not suggested to infer the large-scale magnetic field or density distribution in Milky Way based on the radio morphologies of SNRs.
4. The thermal conduction might slightly influence the SNR radio morphologies, but is not very important.
5. The separation between X-ray and radio emission of some SNRs is possibly related with the motion of the progenitor.

We note that there are many simplifications in our current work. It will be interesting to study the formation of multi-layers and irregular SNRs by more detailed simulation in the near future, e.g. including an inhomogeneous initial surrounding environment or a special progenitor, etc.

We thank Dr.Meyer for his explaining the thermal conduction of the stellar wind. We acknowledge support from the NSFC (11473038).

Software: PLUTO (Mignone et al. 2007, 2012)

REFERENCES

- Bamba, A., Ueno, M., Koyama, K., & Yamauchi, S. 2001, PASJ, 53, L21
- Broersen, S., & Vink, J. 2015, MNRAS, 446, 3885
- Chen, Y., Liu, N., & Wang, Z.-R. 1995, ApJ, 446, 755
- Cioffi, D. F., McKee, C. F., & Bertschinger, E. 1988, ApJ, 334, 252
- Craig, W. W., Hailey, C. J., & Pisarski, R. L. 1997, ApJ, 488, 307
- Fang, J., & Zhang, L. 2012, MNRAS, 424, 2811
- Foster, T., Routledge, D., & Kothes, R. 2004, A&A, 417, 79
- Frail, D. A., Goss, W. M., & Whiteoak, J. B. Z. 1994, ApJ, 437, 781
- Gaensler, B. M., Brazier, K. T. S., Manchester, R. N., Johnston, S., & Green, A. J. 1999, MNRAS, 305, 724
- Green, D. A. 2014, Bulletin of the Astronomical Society of India, 42, 47
- Gvaramadze, V. V., Menten, K. M., Kniazev, A. Y., et al. 2014, MNRAS, 437, 843

- Haverkorn, M. 2015, in *Astrophysics and Space Science Library*, Vol. 407, *Magnetic Fields in Diffuse Media*, ed. A. Lazarian, E. M. de Gouveia Dal Pino, & C. Melioli, 483
- Jun, B.-I., & Norman, M. L. 1996, *ApJ*, 465, 800
- Kang, H., & Jones, T. W. 2006, *Astroparticle Physics*, 25, 246
- Leahy, D. A., & Tian, W. W. 2008, *A&A*, 480, L25
- Leahy, D. A., & Williams, J. E. 2017, *AJ*, 153, 239
- Lee, J.-J., Park, S., Hughes, J. P., et al. 2010, *ApJ*, 711, 861
- Long, K. S., Blair, W. P., Matsui, Y., & White, R. L. 1991, *ApJ*, 373, 567
- Mackey, J., Gvaramadze, V. V., Mohamed, S., & Langer, N. 2015, *A&A*, 573, A10
- Meyer, D. M.-A., Gvaramadze, V. V., Langer, N., et al. 2014a, *MNRAS*, 439, L41
- Meyer, D. M.-A., Langer, N., Mackey, J., Velázquez, P. F., & Gusdorf, A. 2015, *MNRAS*, 450, 3080
- Meyer, D. M.-A., Mackey, J., Langer, N., et al. 2014b, *MNRAS*, 444, 2754
- Meyer, D. M.-A., Mignone, A., Kuiper, R., Raga, A. C., & Kley, W. 2017, *MNRAS*, 464, 3229
- Mignone, A., Bodo, G., Massaglia, S., et al. 2007, *ApJS*, 170, 228
- Mignone, A., Zanni, C., Tzeferacos, P., et al. 2012, *ApJS*, 198, 7
- Müller, B., Heger, A., Liptai, D., & Cameron, J. B. 2016, *MNRAS*, 460, 742
- Nakanishi, H., & Sofue, Y. 2006, *PASJ*, 58, 847
- . 2016, *PASJ*, 68, 5
- Orlando, S., Bocchino, F., Reale, F., Peres, G., & Petruk, O. 2007, *A&A*, 470, 927
- Orlando, S., Drake, J. J., & Miceli, M. 2017, *MNRAS*, 464, 5003
- Pannuti, T. G., Rho, J., Borkowski, K. J., & Cameron, P. B. 2010, *AJ*, 140, 1787
- Petruk, O., Beshley, V., Bocchino, F., & Orlando, S. 2009, *MNRAS*, 395, 1467
- Poznanski, D. 2013, *MNRAS*, 436, 3224
- Schneider, E. M., de La Fuente, E., & Velázquez, P. F. 2006, *MNRAS*, 371, 369
- Su, Y., Chen, Y., Yang, J., et al. 2009, *ApJ*, 694, 376
- Sukhbold, T., Ertl, T., Woosley, S. E., Brown, J. M., & Janka, H.-T. 2016, *ApJ*, 821, 38
- Sun, X. H., Reich, P., Reich, W., et al. 2011, *A&A*, 536, A83
- Tammann, G. A., Loeffler, W., & Schroeder, A. 1994, *ApJS*, 92, 487
- Tian, W.-W., & Leahy, D. 2006, *ChJA&A*, 6, 543
- Toledo-Roy, J. C., Esquivel, A., Velázquez, P. F., & Reynoso, E. M. 2014a, *MNRAS*, 442, 229
- Toledo-Roy, J. C., Velázquez, P. F., Esquivel, A., & Giacani, E. 2014b, *MNRAS*, 437, 898
- Truelove, J. K., & McKee, C. F. 1999, *ApJS*, 120, 299
- van Marle, A. J., Cox, N. L. J., & Decin, L. 2014a, *A&A*, 570, A131
- van Marle, A. J., Decin, L., & Meliani, Z. 2014b, *A&A*, 561, A152
- van Marle, A. J., Meliani, Z., & Marcowith, A. 2012, *A&A*, 541, L8
- . 2015, *A&A*, 584, A49
- van Marle, A. J., Smith, N., Owocki, S. P., & van Veelen, B. 2010, *MNRAS*, 407, 2305
- Vigh, C. D., Velázquez, P. F., Gómez, D. O., et al. 2011, *ApJ*, 727, 32
- West, J. L., Safi-Harb, S., Jaffe, T., et al. 2016, *A&A*, 587, A148
- Yar-Uyaniker, A., Uyaniker, B., & Kothes, R. 2004, *ApJ*, 616, 247
- Zhang, M. F., Tian, W. W., Leahy, D. A., et al. 2017, *ApJ*, 849, 147
- Zhang, Q.-C., Wang, Z., & Chen, Y. 1996, *ApJ*, 466, 808